Science Robotics
AAAS

robotics.sciencemag.org/cgi/content/full/5/40/eaaz0492/DC1

Supplementary Materials for

An untethered isoperimetric soft robot

Nathan S. Usevitch*, Zachary M. Hammond*, Mac Schwager, Allison M. Okamura, Elliot W. Hawkes, Sean Follmer

*Corresponding author. Email: usevitch@stanford.edu (N.S.U.); zhammond@stanford.edu (Z.M.H.)

Published 18 March 2020, *Sci. Robot.* **4**, eaaz0492 (2020)
DOI: 10.1126/scirobotics.aaz0492

The PDF file includes:

Other Supplementary Material for this manuscript includes the following:

(available at robotics.sciencemag.org/cgi/content/full/5/40/eaaz0492/DC1)

Text

S1: Experimental Setup for Measuring Battery Life

The continuous battery life of the prototype presented in this paper is shown in fig. S1A. A triangular robot was oriented vertically and one of its roller modules was driven in a cycle pattern while monitoring the energy delivered it (fig. S1B – S1D). Using the energy consumed and the time elapsed during each cycle, we compute the estimated battery life of the 14.8 V, 1300 mAh, LiPo batteries we use in our demonstrations. These batteries are assumed to store 69.3 KJ of energy which is calculated with the following equation

$$E_{stored} = (1300\ \text{mAh})(14.8\ \text{V})(3600\ \text{sec/h}) = 69.3\ \text{KJ}$$

We note that one of the chief inefficiencies of our design is the motor used in the robot (ServoCity part #638320) exhibit a peak efficiency of less than 30%. Battery life could be substantially improved by using a more efficient motor, or by reducing friction in the custom gear train.

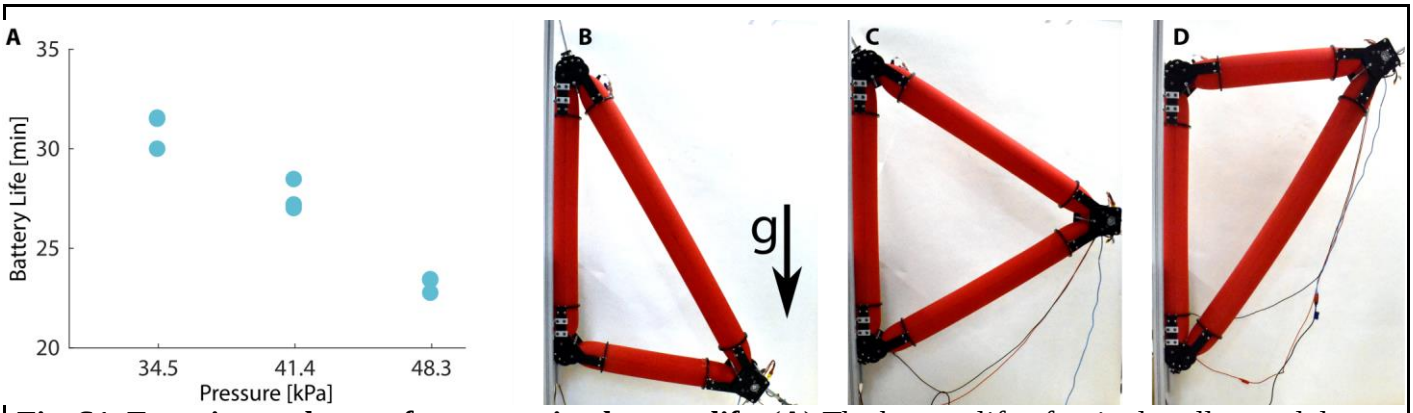

Fig. S1. Experimental setup for measuring battery life. (**A**) The battery life of a single roller module running continuously at three different pressures. We repeated the test three times per pressure. (**B to D**) The roller module is moved in a cyclic path. The roller module is a part of a triangle oriented vertically so that the roller module moves against gravity. The battery life calculated in (**A**) is extrapolated from the energy drawn and time elapsed during one cycle starting at a low point (**B**) moving upward to a high point (**D**) and then returning to the low point (**B**). The battery used for this calculation is a 14.8 V, 1300 mAh, LiPo battery.

S2: Modeling and Measuring Bending of a Beam Through Rollers

We present a reduced order model to measure the torque required to bend an inflated fabric tube around a set of rollers. Our key assumption is that the tube material is flexible but inextensible, and that the tube will take a shape that maximizes its enclosed volume for a fixed joint angle. These assumptions allow us to write $V = f(\theta)$ and calculate the torque using the principle of virtual work $\tau(\theta) = -P\frac{dV(\theta)}{d\theta}$. To use this model requires us to (i) parameterize the shape of the tube, (ii) compute the tube's volume, and (iii) characterize the change in volume with angle. Past work has studied the post-buckling bending response of inflated fabric beams

without rollers (*54-55*), as well as models to predict the force exerted on the rollers when the tube is only inflated on one side of the rollers (*56-57*). Our approach will combine elements of these modeling approaches to quantify the change in torque with the angle of a beam passing through a set of rollers.

Shape Parameterization

We parameterize the shape of the tube as shown in Fig. S2A. We assume that the paths along the top and bottom of the inflated membrane are of equal length, smooth (the derivative is continuous everywhere), and that they are composed of a constant curvature section and a straight section when not in contact with the roller. We wish to express the equation of the top and bottom paths as functions of the geometric constant parameters (D, h, R_{roll}, L_{tot}, θ), and two input parameters of our choice that we will later optimize over. We select R_t and R_b as the input parameters and solve for the values for α_t, α_b , c_t and c_b using geometric constraints. First, we relate the tube diameter to four of the geometric parameters:

$$c_b + c_t + R_t + R_b = D.$$

Examining the geometry defining the constant curvature section of tube near the rollers, we can develop two more equations relating known distances:

$$(R_{Roll} + R_t)\cos(\alpha_t + \theta) + c_t = \left(\frac{h}{2} + R_{Roll}\right)\cos(\theta),$$
$$(R_{Roll} + R_b)\cos(\alpha_b + \theta) + c_b = \left(\frac{h}{2} + R_{Roll}\right)\cos(\theta).$$

For the final equation, we express the constraint that the lengths of the top and the bottom paths are equal. This constraint takes the form of a loop closure equation:

$$\begin{aligned} R_{Roll}\sin(\alpha_t) + R_t\sin(\alpha_t) + R_t\sin(\theta) + \big(L_{tot} - R_{Roll}\alpha_t - R_t(\alpha_t + \theta)\big)\cos(\theta) - D\sin(\theta) \\ = R_{Roll}\sin(\alpha_b) + R_b\sin(\alpha_b) - R_b\sin(\theta) + \big(L_{tot} - R_{Roll}\alpha_b - R_b(\alpha_b + \theta)\big)\cos(\theta). \end{aligned}$$

We solve these interdependent equations numerically which gives us the shape of the top path of the membrane as $\gamma_{top}(\lambda, \theta, R_t, R_b)$ and the shape of the bottom path of the membrane $\gamma_{bottom}(\lambda, \theta, R_t, R_b)$, where λ is a parameter along the arc length of the tube. For clarity, we denote the collection of the parameters θ, R_t, R_b as p. We assume that the cross section of the tube is described by a square in between two half circles as shown in Fig. S2A. The perimeter of this cross section is held constant at πD, meaning that no wrinkles form in the longitudinal direction along the tube. For a fixed value of λ, $\gamma_{top}(\lambda, p)$ and $\gamma_{bottom}(\lambda, p)$ intersect the cross section respectively at the top and bottom of the cross section on the axis of symmetry. We denote the height of this cross section $h(\lambda, p) = \left|\left|\gamma_{top}(\lambda, p) - \gamma_{bottom}(\lambda, p)\right|\right|$, and the normal vector to the cross section $n(\lambda, p)$. Using the assumption that the perimeter of the cross section is constant, we can write

$$A(\lambda, p) = \pi\frac{h(\lambda,p)}{2}\left(D - \frac{h(\lambda,p)}{2}\right).$$

To compute the volume of the tube we define the center path of the tube as

$$c(\lambda) = \frac{1}{2}\left(\gamma_{top}(\lambda, p) + \gamma_{bottom}(\lambda, p)\right)$$

and utilize techniques from (*58*) to write:

$$V(\theta,\ R_t, R_b)\ =\ \int_0^{L_{tot}} A(\lambda, p)\left(\gamma'(\lambda, p) + \big(\gamma(\lambda, p)\ -\ c(\lambda, p)\big)\cdot n'(\lambda, p)\right) d\lambda.$$

We assume that the tube will take the shape that maximizes the volume. We find $V^*(\theta)$ by fixing the value

of θ and maximizing the volume with R_t and R_b as free variables:

$$V^*(\theta) = \max_{R_t, R_b} V(\theta, R_t, R_b).$$

Computing the Model

We solve the problem of maximizing the volume using the Matlab fmincon optimization solver. A few of these optimized shapes are shown in Fig. S2B. To obtain $\frac{dV}{d\theta}$ we compute $V^*(\theta)$ and obtain the gradient with angle through a finite difference.

We note that in the actual structure there may be axial and bending loads on the robot which would affect the shape of the beam. While it may be possible to use a similar approach and parameterization of the shape to predict the response in these cases, doing so is beyond the scope of this work. In the current form, the model captures the trend and approximate magnitude of the response and is sufficient for design purposes. Another key component of the model is the ability to predict the onset of self-interference. Our model does not predict the effect of tube self-interference on joint stiffness, but it does predict when self-interference occurs.

Experimental Setup

We experimentally measure the angle and torque of the beam using the setup shown in Fig. S2C. We use 70 denier ripstop nylon fabric with a polyurethane coating to form a tube with a seam created with a line impulse sealer. The tube is secured to a frame built from aluminum extrusions by two polyoxymethylene (POM) rings. We measure the angle using a digital goniometer. We built a roller apparatus with rollers of 0.635 cm, 1.27 cm, and 2.54 cm. For all conditions the minimum distance between the rollers was 0.049 cm. We measure the force using a Mark-10 load cell rigidly attached to a POM ring sized precisely to the tube which we maintain normal to the beam. We compute the torque by multiplying the measured force by the distance from the rollers to the load cell. We control the pressure in the beam using a closed loop pressure control. We incrementally increase the angle and measure the torque, allowing time for pressure to settle to a nominal value.

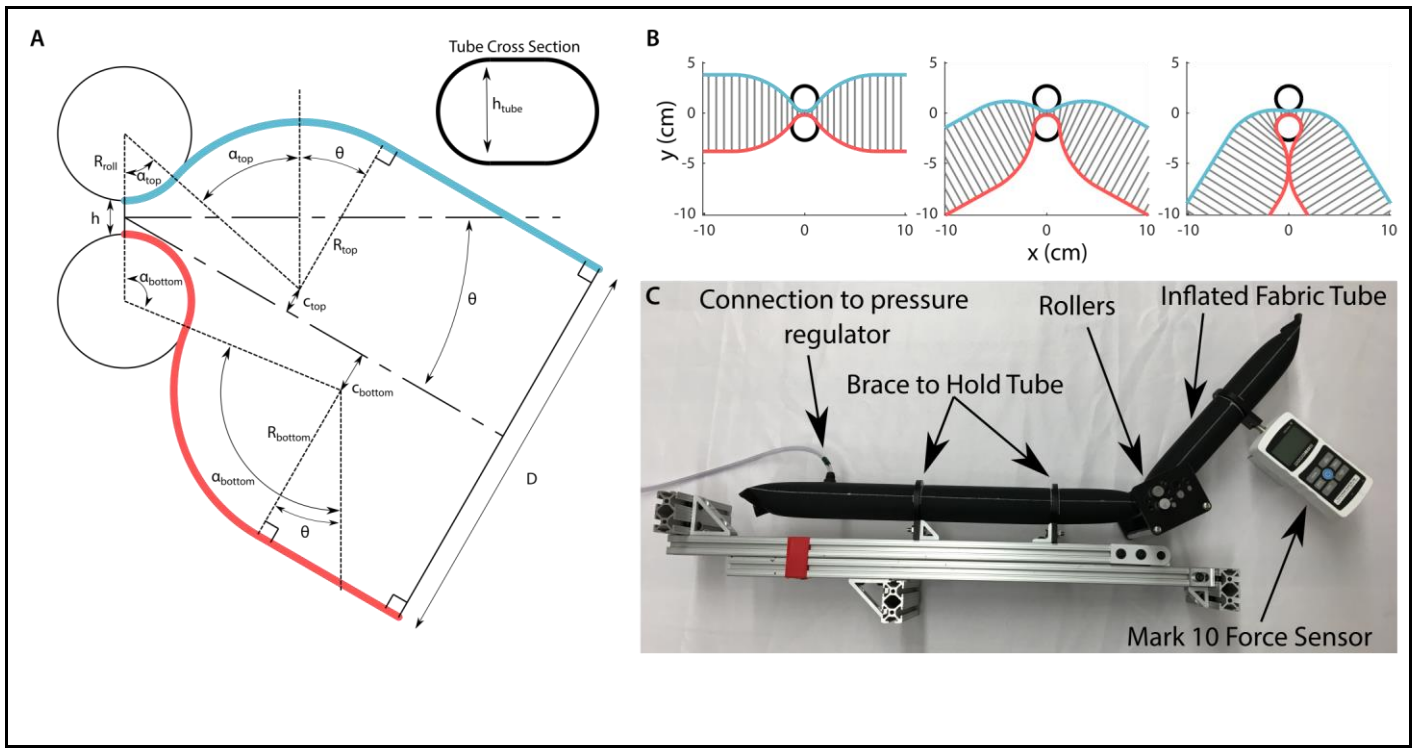

Fig. S2. Torque angle relationship for a beam between rollers. (A) Parameterization of the resulting shape of the tube as it passes through the rollers. We assume that the top and bottom path along the tube take a continuous path with two constant curvature segments. **(B)** The optimized shapes of the tube when straight, at an intermediate angle, and at the configuration where the membrane begins to self-intersect. **(C)** The test setup used to collect the data we used to compare with the model.

S3: Model Predictions of the Normal Force Between Rollers

In addition to allowing us to compute the torque required to bend to a certain angle, the same shape parameterization presented in section S2 also allows an estimation of the magnitude of the force exerted by the tube that pushes the rollers apart, which we refer to as the normal force or F_N. This force is necessary for traction yet can cause the rollers to bend. Here we define the volume as a function of the gap distance, h, and assume that the angle is specified. Using the principle of virtual work, $F_N(h,\theta) = P\frac{dV(h,\theta)}{dh}$, which allows us to quantify the force acting to separate the rollers. Fig. S3A shows the normal force as a function of the angle at different roller diameters, and fig. S3B shows the normal force as a function of angle at different tube diameters. In general, the magnitude of the normal force decreases with angle, but overall is quite large in magnitude. In our experiments the magnitude of these forces has been sufficient to resist slipping between the tube and the rollers.

Using the normal force data from fig. S3 we can predict the bending stress within the rollers. Assuming a normal force, $F_N = 250\ N$, that is evenly distributed along the length of the roller and that the roller is fixed at both ends, we can calculate the maximum bending stress to be:

$$\sigma_{max} = \frac{64F_N d_T}{d_R^3} = 460\ MPa$$

where the tube diameter, $d_T = 10.1\ cm$ and the roller diameter, $d_R = 1.52\ cm$. Many steels have fatigue limits in the range of $400 - 900\ MPa$ (*59*). Therefore, we can design the roller modules to be robust to cyclic loading.

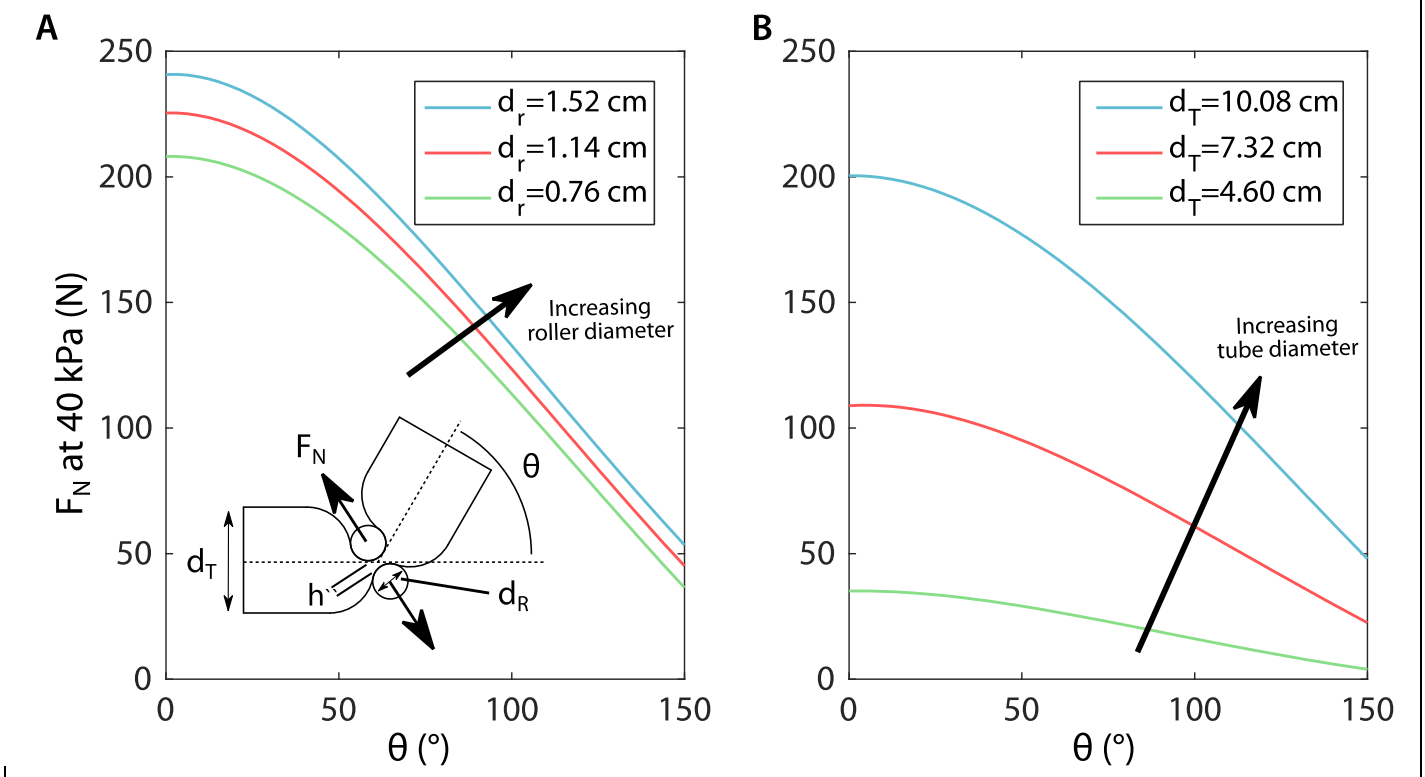

Fig. S3. Model predictions of the normal force between rollers. (A) Model results for the normal force between two rollers at different angles and with different roller diameters. The diameter of the tube is constant at 10.08 cm. The normal force decreases with angle, and larger rollers lead to larger normal forces. **(B)** The normal force between rollers predicted by the model with different tube diameters. The rollers have a constant diameter of 0.76 cm. Increasing the tube diameter increases the normal force.

S4: Experimental Setup for Analyzing Cost to move along Rollers

The apparatus shown in fig. S4 was used to collect the force required to move the tube with respect to the rollers. We use 70 denier ripstop nylon fabric with a polyurethane coating to form a tube with a seam created with a line impulse sealer. A series of laser cut plates held together with aluminum extrusions and standoffs locate the roller bearings and a winch system used to transmit force from a force sensor to the rollers. A pull string is connected to the Mark-10 force sensor. As the load cell is pulled, the winch system rotates one of the rollers through a belt and two pulleys. The other roller is free to spin and rotates with the driven roller because the tube presses securely against both rollers. We use three different roller diameters of 0.76 cm, 1.14 cm, and 1.52 cm. We tested three tube diameters of 4.60 cm, 7.32 cm, and 10.08 cm. For all conditions the minimum distance between the rollers was 0.049 cm. We control the pressure in the beam using a closed loop pressure control.

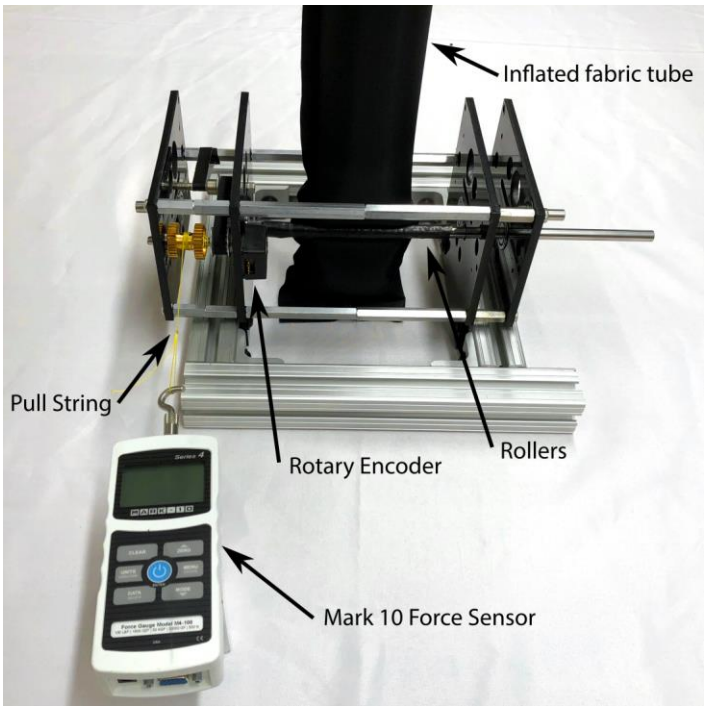

Fig. S4. Test apparatus to quantify cost of motion. Test apparatus used to measure the force required to overcome friction and move the tube through the rollers. An inflated tube was placed within the rollers and a force sensor was used to apply a torque on a shaft that was coupled to one of the rollers with a belt and pulleys. The entire length of the tube was slowly pulled through the rollers and the force required to move the rollers was averaged.

S5 Deformation of an Individual Triangle

We measure the response of a single triangle to an externally applied load using the experimental setup in fig. S5. The passive module of the triangle is secured to a carriage free to move on a linear track. The other two roller modules are supported by a long brace and are positioned such that the linear track bisects the inner angle formed by the inflated tube at the passive module. The Mark-10 force sensor is pushed into the passive module along the linear track until the triangle completely collapses. A linear encoder tracks the position of the carriage as it moves. The Mark-10 is then moved backwards along the track as the edges of the triangle begin to straighten and exert a restoring force on the force sensor. We test three isosceles triangles: obtuse (edge lengths of 89 cm, 89 cm, and 128 cm), equilateral (edge lengths of 102 cm), and acute (edge lengths of 121 cm, 121 cm, and 64 cm). The initial pressure is set using a closed-loop pressure control and was set at 41.4 kPa. At the beginning of the test, a valve is closed such that the tests are performed with a fixed mass of air within the tube.

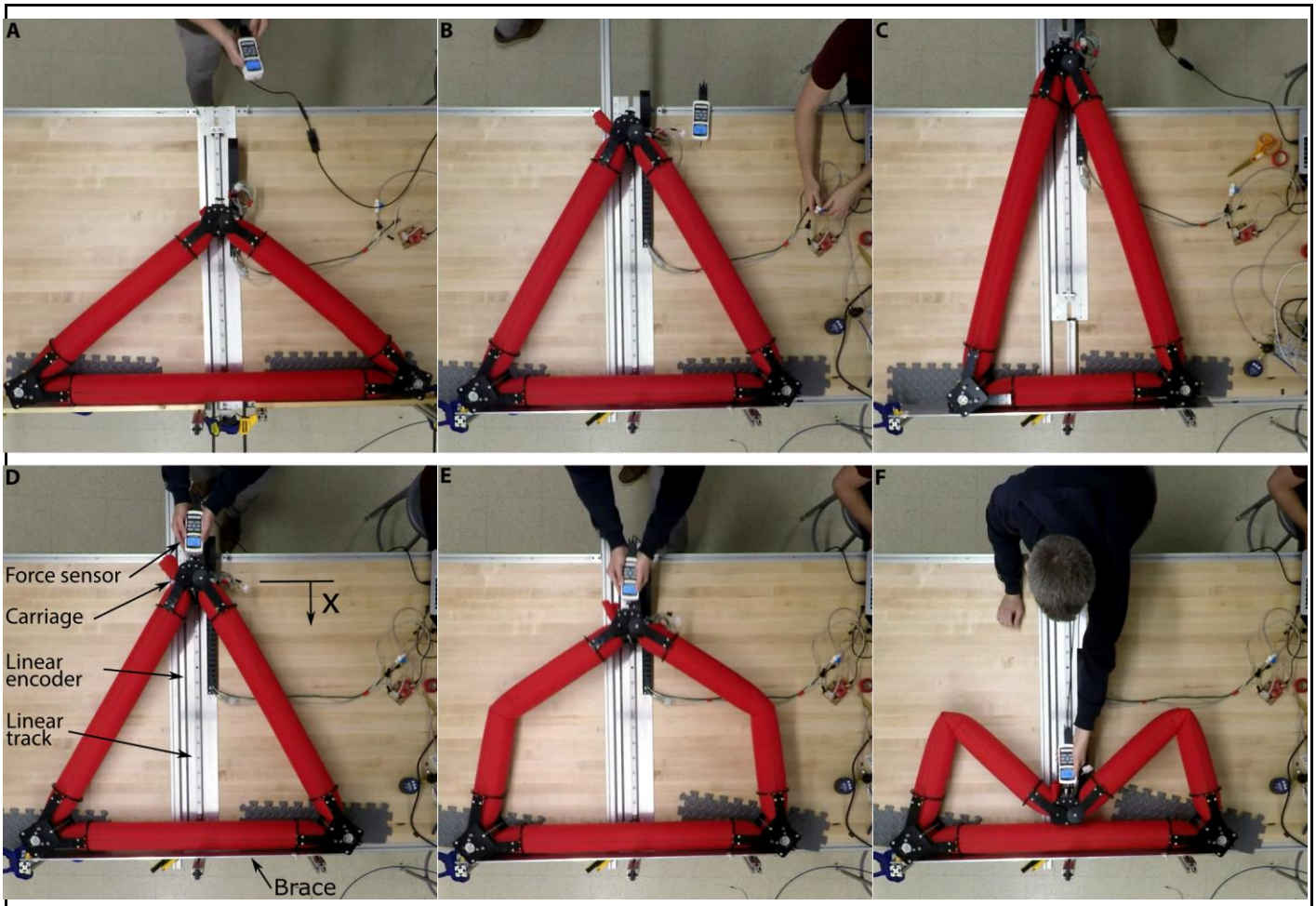

Fig. S5. Deformation of an individual triangle. Measurement of the force/displacement relationship of a single triangle. The top row of images shows three different configurations the triangle was tested in. **(A)** Obtuse triangle (edge lengths of 89 cm, 89 cm, and 128 cm). **(B)** Equilateral triangle (edge lengths of 102 cm). **(C)** Acute triangle (edge lengths of 121 cm, 121 cm, and 64 cm). The bottom row of images shows the equilateral triangle (B) being loaded. **(D)** The triangle is initially stiff to external loads. **(E)** With a sufficiently large load the triangle buckles. **(F)** The triangle at maximum displacement.

S6 Roller Module Design

A part callout of the roller module is presented in Fig. S6. The roller module is fabricated from POM sheets separated by steel hexagonal standoffs. All electronic components, as well as the node connection components are attached to the top plate of the roller module. A key structural challenge is managing the large forces required to pinch the fabric tube which are modeled in S3. While this force is supported by the structure of the roller module itself, these forces can be extremely large and the steel rollers that we utilize bow visibly in our current system.

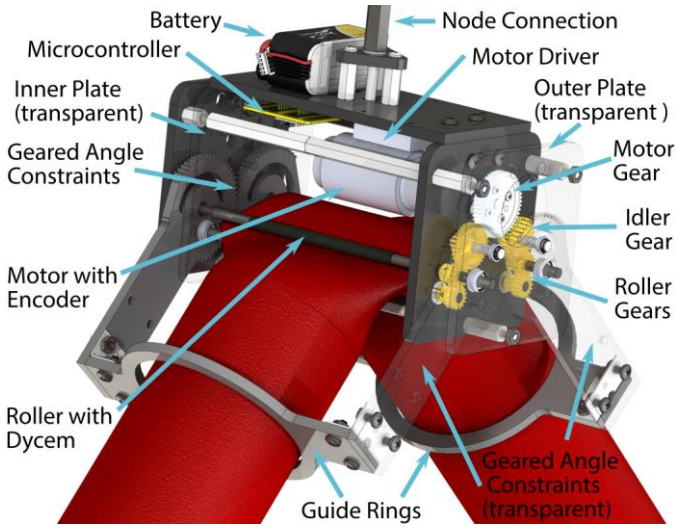

Fig. S6. Mechanical design of roller module. Four parts in this figure are falsely transparent so that other parts can be shown. The outer plate on the right-hand side and the two geared angle constraints on the right-hand side are transparent so the transmission can be seen. The inner plate on the left-hand side is transparent so the geared angle constraints can be seen.

S7: Descriptive Figure for the kinematics

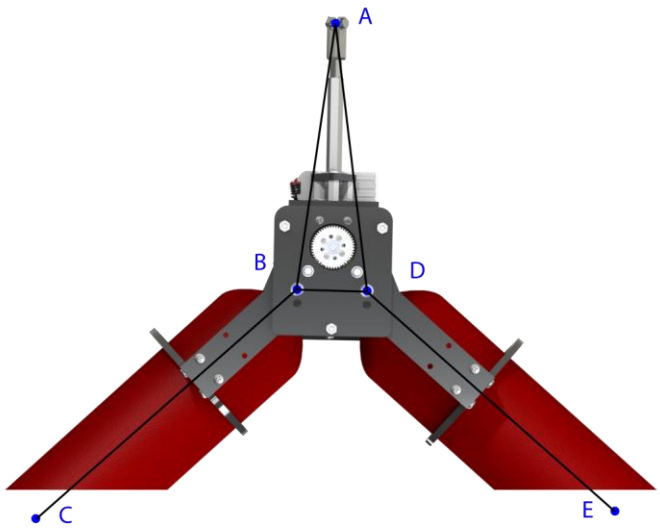

Fig. S7. Diagram of points used to define the kinematics of each roller module. An illustration of the three points at each roller module that are used to represent the state of the robot. Point A is the connection between two roller modules. Points B and D are the center points of the rollers. Points C and E are the opposite ends of the respective edges.

S8: Comparison with other robots

In simulation we compare the efficiency and speed of an idealized isoperimetric robot and a truss robot composed of two actuators mounted at pin joints. Specifically, we compute the energy required to move Node 2 of robot A and C in Fig. 8 and Fig. S8 between a set of waypoints in a prescribed amount of time. The waypoints are randomly generated within a square region superimposed within the shared workspace of the two robots (fig. S8D). We assume that each node is a point mass of 2.63 kg, and that the edges have no mass. We first define the motion by specifying that Node 2 move in a straight line between waypoints, following the velocity profile shown in fig. S8E. We then utilize the kinematics presented in Materials and Methods to compute the forces and speeds required from the robot actuators to create the motion while the robot is subject to both inertial and gravitational loads. Given the torques and speeds of the actuators, we compute the total output energy for the actuators as $(\int \tau(t)\omega(t)dt)$. Fig. 8E shows that the isoperimetric robot requires slightly less energy at low frequencies, but higher amounts of energy at higher frequencies. For a prescribed motion of Node 2, Node 3 of the isoperimetric robot must also move to maintain the constant perimeter. The additional motion of Node 3 is increasingly costly as frequency increases and dynamic effects become more pronounced.

We also compare the efficiency and speed for different power sources. Given the speed and torques required from the actuators, we can determine the amount of energy that must be input to the system given an actuator choice of a specific motor or microcompressor. We compute the input power as $(\int V(t)i(t)dt)$ where $V(t)$ and $i(t)$ are the supplied voltage and current for either the motor or the microcompressor. As our representative motor we select the Actobotics 52 RPM (#638296) premium planetary gear motor (231.22:1 gear ratio, mass of 118 g). For the microcompressor we select the Parker Hargraves BTC-IIS

microcompressor (170 g) due to its characterization in past studies and its similar weight to the motor (*40*). In the case of the microcompressor, we must relate the linear motion and force of the pneumatic cylinder to the pressure and flow rate at the microcompressor. We assume that the piston has constant diameter such that $PA = F$.

Examining the closed volume within the cylinder and assuming an isothermal process, we write the following

$$PV = mRT$$
$$\dot{P}V + P\dot{V} = \dot{m}RT$$
$$\dot{m} = \frac{1}{RT}\left(\frac{dF}{dt}L + P_g + P_{atm}\dot{L}A\right)$$

This allows us to compute the flow rate required at the microcompressor given a time history of pressure and length of the actuator, which together with the microcompressor parameters allows us to compute the input energy.

We compare the required input energy to move the robot between waypoints. We compare robot A in Fig. 8 with two different types of robot C: one of linear actuators driven by motors and one of pneumatic cylinders driven by microcompressors (Fig. 8F). Across all of the time scales studied, the input power required by the isoperimetric robot is higher than for the motor-driven robot composed of linear actuators. Both motor driven systems complete the trajectories in a minimum time of 11 seconds, while the microcompressor-based system takes 273 seconds to complete the trajectory. We note that the energy required increases faster for the motor driven system then for the microcontrollers, such that the energy required switches at low speeds. This is because at slow speeds the motors are far from operating at their most efficient condition. We also note that for the idealized motor-driven system where the motors are perfectly backdrivable, the motors must exert a holding torque to keep the end effector at rest. For the pneumatic system, no energy is required to hold the system at a stationary condition. These results indicate that the motor driven system has the potential for faster and more efficient operation at moderate speed scales.

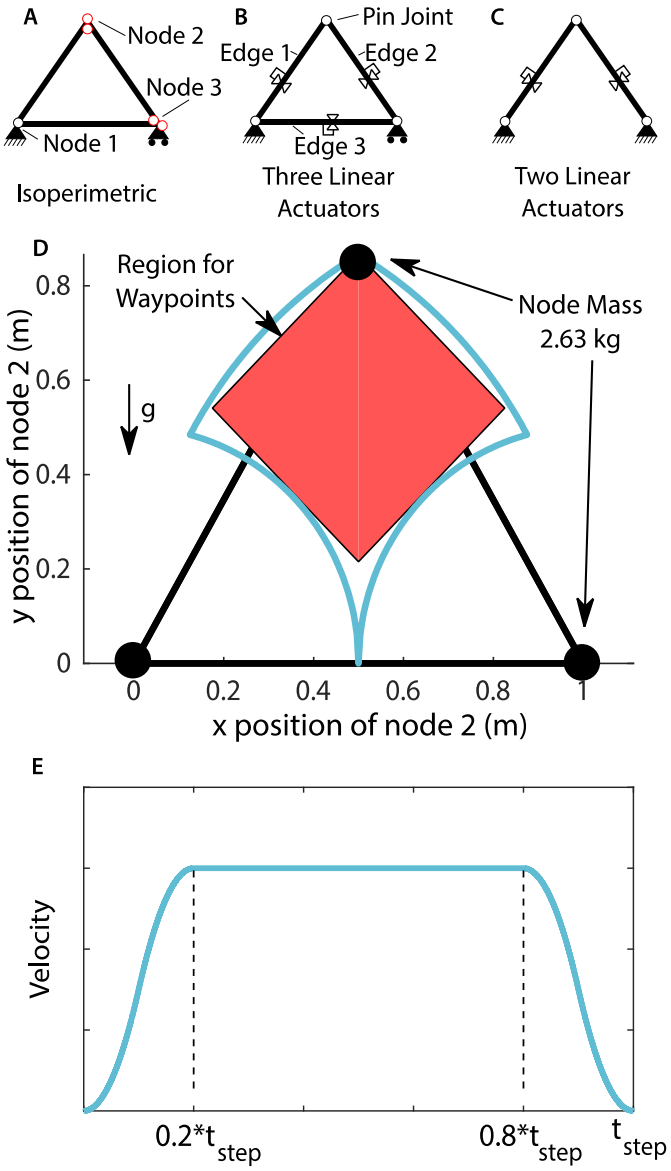

Fig. S8. Details of the comparison with different truss robots. Comparison of the energy required to move robots (**A**), (**B**), and (**C**) between waypoints. (**D**) The robots move Node 2 to waypoints that are randomly generated within the square superimposed within the shared workspace of the robots. The node moves in a linear path between the waypoints according to the velocity profile shown in (**E**).

Movie S1. Motion of the roller module along an inflated tube.
This movie shows close-up shots of the roller module. The first segment shows how the rollers drive along the inflated tube like wheels. The camera is fixed with respect to the roller modules. As the motor drives the rollers, the striped tube appears to move through the rollers. In the second segment the roller module moves along an inflated tube that is pinned to the ground at its ends and forms a triangle. The camera is fixed with respect to the ground. As the roller module moves, the shape of the triangle changes as one edge shortens and the other lengthens. In the final segment, we see how the guide rings are constrained to move together due to the geared angle constraints.

Movie S2. Inflation and shape change of a 2D robot.
A 2D robot composed of three separate inflated tubes is demonstrated in this movie. The inflated tubes are formed into triangles with two active roller modules and one passive module. The triangles are then connected to each other to form this robot. The robot is initially deflated and inflates into an equilateral triangular shape. After the operating pressure is reached, the robot is untethered from the external compressor. At this point the roller modules move along the inflated structure to change the shape into an obtuse triangle, hexagon, acute triangle, square, and a pincer that can grasp a basketball.

Movie S3. Operation of a single-tube 2D robot.
A 2D robot composed of just a single inflated tube is demonstrated in this movie. To shorten and lengthen the two edges adjacent to an active roller module, that active roller module simply drives along the tube. To change the adjacent edge lengths of the passive module with a similar connectivity, all of the active roller modules in the network must drive to preserve the other edge lengths. With this network, there is only a single length constraint for the entire network and any two edges can trade length. In this movie we also see how we can make some edges extremely long by reducing the length of other edges in the network.

Movie S4. Shape change of octahedron robot.
This movie demonstrates the octahedron robot changing shape in interesting ways despite the constant length constraints. The first segment shows how the structure can twist. The second segment shows the structure growing tall, spreading flat and short, and extending one of its nodes out to the side. As the robot moves from one configuration to the next, the structure takes some unintuitive intermediate shapes due to the unique construction of this robot. In general, edges connecting two active roller modules can change length twice as fast as edges connecting a passive module and an active roller module.

Movie S5. Comparison of predicted and measured motion.
This movie conceptually compares the observed motion of the robot to the predicted motions from the kinematic simulation. The commands used as inputs to the simulation are the same commands that were sent to the robot in the experiment, and we assume that each roller module moves along the tube at a constant speed. While the simulation does not account for the deflection and dynamic motions that occur in the actual experiments, it does capture the character of the movement.

Movie S6. Octahedron robot locomotes with a punctuated rolling gait.
This movie demonstrates a 3D robot constructed with the same roller modules used for the 2D demonstrations. Four separate inflated tubes are formed into triangles with two active roller modules and one passive module. The four triangles are then connected together to form an octahedron structure with planar faces. The shape of the structure changes as the roller modules drive along the inflated tubes. This shape change enables locomotion of the robot with a punctuated rolling gait. The same demonstration was filmed from two perspectives. We also show the robot locomoting while untethered in an outdoor environment.

Movie S7. Compliance and interaction of the robot with people.
This movie demonstrates the inherent compliance of the robot as it interacts with people. In the first movie a user applies loads by pushing on the robot. Under all loads, the structure exhibits some softness due to the compliant nature of the beams. If the user applies a large force on the beam, the inflated beams will buckle, reducing the force required by the user to maintain a given level of deflection. This gives the structure a behavior similar to that of a mechanical fuse. When the load is released from a buckled configuration the robot will occasionally recover to the nominal configuration on its own but will sometimes require an external load to return to the nominal configuration. The robustness of the robot is demonstrated as no permanent damage is caused by this buckling. In the second movie two users interact with the robot by carrying it, rolling it around, causing it to buckle, climbing inside the robot, and standing on some of the edges of the robot that are on the ground while the robot is in operation.

Movie S8. Octahedron robot moving a payload.
In this movie the octahedron robot moves back and forth while two metal plates with a mass of 6.8 kg are attached to the joint between two roller modules. This demonstrates the ability of the robot to apply large forces. Due to the parallel structure of the robot, in this case two different motors contribute to moving the mass.

Movie S9. Simulated loading with payload.
This movie shows a simulation of the octahedron robot moving back and forth while a 66.7 N load (indicated by the arrow) is applied at one of the connections between roller modules. Also included in the load is the weight of each roller module. The color of each edge corresponds to the loading condition, where negative values for the axial forces correspond to compressive loads. The

kinematics presented in the materials and methods section are used to compute the Jacobian, which is used to simulate the motion from actuator inputs, as well as reconstruct the axial loads on the edges under the given loading condition. These results are for a quasi-static case, meaning there are no dynamic effects.

Movie S10. Self-recovery from buckling.
This movie illustrates two different strategies that allow the octahedron robot to recover from a buckled configuration. In the first case, a roller module connected to the buckled edge moves towards the buckle point, eventually straightening the beam as the buckle point enters the roller module. In the second case, we move the other roller modules in the network to reduce the load on the buckled edge, allowing the restoring forces within that buckled beam to straighten that edge.

Movie S11. Manipulation.
This movie illustrates the robot using the inherent compliance to interact with objects. First the robot grasps a basketball by moving over it to engulf it, pinching it between two of the inflated beams, and then changing shape to lift the basketball. Second, the movie shows that when a basketball is placed between two beams, motion of the roller modules can cause the basketball to rotate while the grasp is maintained. Third, a bucket of ball is handed off to the robot, which then changes shape to dump out the bucket.

Movie S12. Reachable workspace for a single triangle.
This movie illustrates the theoretical workspace of the top node of a triangle robot built from a single tube using our concept. The top node traces the boundary of the workspace. The tube is of length 3 units, and the minimum allowable edge length is .5 units. The bottom left node of the triangle is fixed, and the bottom right node of the triangle is fixed in the vertical but not the horizontal direction.